A&A 476, 199–215 (2007)
DOI: 10.1051/0004-6361:20077210

Astronomy & Astrophysics

NTT and VLT diffraction limited imaging of Trumpler 14: revealing a massive core-halo cluster⋆,⋆⋆

J. Ascenso[1,2], J. Alves[3], S. Vicente[4], and M. T. V. T. Lago[1,2]

[1] Centro de Astrofísica da Universidade do Porto, Rua das Estrelas, 4150-762 Porto, Portugal
e-mail: joanasba@astro.up.pt
[2] Departamento de Matemática Aplicada da Faculdade de Ciências, Universidade do Porto, Rua do Campo Alegre 657, 4169-007 Porto, Portugal
[3] Calar Alto Observatory–Centro Astronómico Hispano-Alemán, C/ Jesús Durbán Remón 2-2, 04004 Almeria, Spain
[4] Faculdade de Ciências da Universidade de Lisboa, Campo Grande, 1749-016 Lisboa, Portugal

Received 31 January 2007 / Accepted 31 July 2007

ABSTRACT

Aims. We present the deepest and highest resolution near-infrared imaging to date of cluster Trumpler 14 in Carina. Our goal is to identify and characterise the young stellar population of this massive cluster.
Methods. We made use of deep and wide-field NIR images from NTT and VLT observations, that were sensitive enough to detect substellar sources at the distance to this cluster, and at high enough resolution (VLT diffraction limited) to fully resolve the core of the cluster crowded with O stars.
Results. We find that Tr14 has a well-defined core-halo structure, where less than 30% of the cluster's members reside in the core. The core is well characterised by a King function with a core radius of 0.″17 (0.14 pc at the adopted distance) and a constant baseline, the halo, of 125 sources/pc^2. Despite the unusually large number of OB stars, the central number density at zero radius is $\sim 7.3 \times 10^3$ pc^{-3}, which is loose in comparison with similar clusters. We find a normal reddening law towards the cluster and derive a global reddening of $A_v = 2.6 \pm 0.3$ mag. We find convincing evidence of a sparse foreground population ($\sim$5 sources/arcmin^2) reddened by about $A_v = 1.4$ mag, which we suggest is not associated with Tr14 but is most likely an older population produced in the nearby young clusters of this complex. The colour–magnitude diagrams are compatible with ages between "zero" and $\sim$5 Myr, although the sources from the core of the cluster appear to concentrate on the youngest isochrones, suggesting that the halo population is, on average, slightly older than the core population. Using a set of simplistic, fixed-age, mass-luminosity relations, we derive a mass of 10^4 $M_\odot$ for the cluster. From the NACO JHK_sL' data, we estimate a fraction of infrared-excess sources of 35%, although this is likely to be an underestimate given the bright completeness limits of the L' band. Finally, we argue that the formerly identified proplyd candidates that fall inside our survey are not proplyds but remnants of the disrupted molecular cloud that surround the cluster. We also find a series of interesting objects in our field that are worthy of future attention: a candidate photoionised proplyd best seen in the L' band, a compact nebula surrounding an early type star, and a tentative proplyd/small shock associated with a faint source.

Key words. HII regions – open clusters and associations: individual: Trumpler14 – stars: formation – infrared: stars

1. Introduction

Trumpler 14 (Tr14) is one of the most studied clusters in the Galaxy. It is located in the Carina Nebula (NGC 3372) and has an impressive massive star content. It contains no less than 13 O stars, one of which is a rare O2If* (Walborn et al. 2002), and 18 B stars (Massey & Johnson 1993; Vazquez et al. 1996). The presence of such massive, unevolved objects suggests a young age for the cluster ($<10^6$ yr, Morrell et al. 1988; Penny et al. 1993; Massey et al. 2001), which is confirmed by the fitting of evolutionary tracks to optical and near-IR (NIR) photometric data (Feinstein et al. 1973; Carraro et al. 2004; Vazquez et al. 1996; DeGioia-Eastwood et al. 2001; Tapia et al. 2003) and by the presence of a pre-main-sequence (PMS) of fainter stars (DeGioia-Eastwood et al. 2001; Carraro et al. 2004). Vazquez et al. (1996), DeGioia-Eastwood et al. (2001), and Tapia et al. (2003) suggest star formation started 5 to 10 Myr ago and has been active in the cluster since then, and other authors indeed find compelling evidence for ongoing star formation in the whole Carina complex (Megeath et al. 1996; Brooks et al. 1998; Smith et al. 2003, 2004, 2005b; Rathborne et al. 2004). In particular, the Car I dark cloud (de Graauw et al. 1981; Brooks et al. 1998) that borders Tr14 to the SW seems to be an active region of star formation judging by its clumpy structure (Brooks et al. 2003; Tapia et al. 2006) and the presence of deeply embedded (young) objects and ultra-compact HII regions, at least one of which is compatible with a B0-O9 star (Brooks et al. 2001; Rathborne et al. 2002; Tapia et al. 2003). Smith et al. (2003) also find numerous proplyd candidates in the area of Tr14.

Morphologically, Tr14 is a centrally concentrated cluster, roughly spherical in the optical and slightly elongated toward the SW as traced by the NIR (Tapia et al. 2003) and X-rays (Townsley 2006). Tapia et al. (2003) find the cluster population to be abruptly truncated in the SW at the location of the bright rim comprising the ionisation front Car I-E. The cluster is still wrapped in the (original) Northern Molecular Cloud to

⋆ Based on observations collected with the NACO instrument at the VLT/UT4 Yepun at Paranal Observatory, Chile, under ESO program 74.C-0401(A), and with the SOFI instrument at the NTT at the La Silla Observatory, Chile, under ESO program 076.C-0884(A).

⋆⋆ Photometric data are only available in electronic form at the CDS via anonymous ftp to cdsarc.u-strasbg.fr (130.79.128.5) or via
http://cdsweb.u-strasbg.fr/cgi-bin/qcat?J/A+A/476/199

the west and in the back and is in the process of disrupting it by carving an ionised cavity (de Graauw et al. 1981; Brooks et al. 2001). According to Tapia et al. (2003), this cloud should be thick enough to block the light of the background stars in the optical and also in the NIR, acting as a shield against most of the contamination from background sources.

Despite the numerous and different attempts, the distance to the Carina Nebula in general and to Tr14 in particular has not been settled. The first determination of distance goes back to Becker (1960), who estimates a distance to the complex of 1.66 kpc via photographic plate photometry. The distance determinations that followed relied upon spectral parallax from optical and/or NIR photometry (Walborn 1973; Turner & Moffat 1980; Morrell et al. 1988; Tapia et al. 1988; Massey & Johnson 1993; Tapia et al. 2003) and proper motion studies (Cudworth et al. 1993), and have yielded values in the range 1.7 to 3.9 kpc. The measurements that rely solely on optical data are greatly dependent on the accurate knowledge of the extinction law. Several authors (Feinstein et al. 1973; Herbst 1976; Forte 1978; The et al. 1980; Smith 1987; Tapia et al. 1988; Garcia et al. 1988) have reported anomalies in the characteristics of the interstellar reddening in this region, although they seldom disagree amongst themselves on the exact slopes of the reddening vector. Turner & Moffat (1980) and Massey & Johnson (1993), in turn, find no evidence for such anomalies. This issue has contributed for the great discrepancies found in the distances toward Tr14: Feinstein et al. (1973), for example, find distances of 2.6 or 3.4 kpc just by using different extinction laws. This controversy appears to be constrained to optical wavelengths (in particular U and B bands), as the reddening for $\lambda > 0.5$ μm goes back to being "normal" (Tapia et al. 1988).

The issue of whether Tr14 lies at the same distance as the other clusters in Carina, namely Trumpler 16, the other massive cluster of the complex and home to the emblematic luminous blue variable η Carinæ, has also been the subject of strong debate (see Smith et al. (2000) for the spatial context of the Carina nebula). Whereas some authors have argued in favour of the two clusters belonging to the same complex (Becker 1960; Feinstein et al. 1973; The et al. 1980; Tapia et al. 1988; Cudworth et al. 1993; Massey & Johnson 1993), others have placed them at different heliocentric distances (Walborn 1973; Morrell et al. 1988; Carraro et al. 2004) and considered them to be unrelated, usually finding Tr16 to be closer (and also older) than Tr14. In the recent literature, the two clusters are assumed to be at the same distance and associated with same cloud, with the exception of Carraro et al. (2004) who find a much larger distance (4 kpc) for Tr16, based on MS fitting in optical colour–magnitude diagrams.

The goal of this paper is to characterise Tr14 through the deepest and highest resolution NIR survey of this cluster to date. Section 2 describes the data, Sect. 3 presents the results and Sect. 4 lists our most important conclusions.

2. Data

Tr14 was imaged with SOFI, NTT (La Silla, Chile) and with NACO, VLT (Paranal, Chile). In this section we describe the acquisition, reduction and photometry of these data.

2.1. SOFI

The data from SOFI were obtained in the night of March 24, 2006. The cluster ($10^{\rm h}24^{\rm m}01^{\rm s}$, $-57°45'32''$) was imaged in J, H and $K_{\rm s}$ with long exposures for the photometry of the faint stars and short exposures for the bright stars.

The long exposures (12×10 s in J and H and 15×8 s in $K_{\rm s}$) were taken in large field mode (field of view of $4\farcm9 \times 4\farcm9$, pixel scale $\sim 0\farcs288$/pixel) to image the largest possible area of the cluster. The short exposures were taken in large field mode (5×1.2 s for J, H and $K_{\rm s}$) and in small field mode (field of view of $2\farcm4 \times 2\farcm4$, resolution $\sim 0\farcs144$/pixel, 5×1.2 for J, H and $K_{\rm s}$) to image the inner part of the cluster. The shorter exposure times, associated with the distinct (less sensitive) optics configuration in the case of the small field mode, help to minimise the saturation of the brightest stars, mostly concentrated in the central part of the cluster.

We also observed a nearby control field ($10^{\rm h}38^{\rm m}13^{\rm s}$, $-59°12'00''$), which lies at approximately the same galactic latitude. This field was imaged in large field mode in J, H and $K_{\rm s}$ with the same (long) exposure times as for the science frames.

2.1.1. Data reduction

The SOFI data was reduced with IRAF[1] following the standard procedure: crosstalk, flatfield and illumination correction. Since the surroundings of the cluster still have a large number of objects, the median filtering applied to the sky frames did not eliminate all the stars, even with threshold pixel rejection and despite the observations having been carried in "on-off" mode, which produced a sky image for every science frame. For this reason we chose to remove the stars in the sky frames via crude PSF subtraction and only then combine the PSF-subtracted sky images adjacent to each science frame to produce representative and homogeneous sky frames adequate for the sky subtraction. The PSF subtraction of the stars in the sky frames introduces a low level of noise that is then carried into the science frames, but our tests showed this to be the best way to perform the sky subtraction with the available images. The individual science subframes were then registered and averaged into the final images.

The offsets between the sub-frames were determined with JITTER. The final J, H and $K_{\rm s}$ frames were then registered to one another. The common area of the images is $3\farcm89 \times 3\farcm81$ for the long exposures, $2\farcm21 \times 2\farcm12$ for the small-field short exposures, and $4\farcm25 \times 4\farcm14$ for the large-field short exposures.

Figure 1 shows the colour image of the cluster composed from the three final long exposure frames in $K_{\rm s}$ (red), H (green) and J (blue).

2.1.2. Source extraction and photometry

We used IRAF DAOFIND to detect the sources in the images. In the long-exposure frames, the routine searched for sources with a PSF of full width at half maximum (*FWHM*) from 2.3 to 2.5 pixels ($0\farcs66$ to $0\farcs71$) and brighter than 5 times the mean noise of each image. For the large-field short-exposure images the *FWHM* ranged from 2.2 to 2.6 pixels ($0\farcs63$ to $0\farcs75$), and the detection threshold was chosen to be 20 to 40 times the mean noise in each image. For the small field short exposure images the *FWHM* was 5.5 pixels ($0\farcs79$) for all bands and the detection threshold was taken as 30 to 60 times the mean noise in each image. The detection threshold in the short exposures is high because we are only interested in the brightest stars that appear saturated in the long exposures that detect the fainter stars at better signal-to-noise ratios.

[1] IRAF, *Image Reduction and Analysis Facility, is distributed by the National Optical Astronomy Observatory (NOAO),* `http://iraf.noao.edu`

Fig. 1. Colour composite of the long-exposure observed field of view in J (blue), H (green) and K_s (red). North is up and east is to the left.

We performed PSF photometry on the stars of the cluster due to crowding in most of the image. This was done with IRAF DAOPHOT. The PSF was chosen from the standard functions defined within IRAF to be the best fit to a set of bright and isolated stars. The best fit was found for the "Penny" function (a Gaussian core with Lorentzian wings) for all bands of all frames except for the J and H bands of the large field, short exposures, where the best fit to the PSF was obtained for the Moffat function (a modified Lorentzian function). The instrumental magnitudes were converted into the Persson et al. (1998) photometric system and from there to the 2MASS photometric system according to the following set of equations:

SOFI to Persson (SOFI's user manual):

$$K_P = 1.005(K_s - 0.005J) \quad (1)$$

$$J_P = J - 0.007(J - K_P) \quad (2)$$

$$H_P = H - 0.022(J - K_P) \quad (3)$$

$$(K_s)_P = K_s + 0.023(J - K_P); \quad (4)$$

Persson to 2MASS (Carpenter 2001):

$$(K_s)_2 = (K_s)_P - 0.002(J_P - (K_s)_P) - 0.01 \quad (5)$$

$$H_2 = 1.019H_P - 0.017(K_s)_P - 0.002J_P - 0.005 \quad (6)$$

$$J_2 = 1.005J_P - 0.005(K_s)_P - 0.008, \quad (7)$$

where the subscripts "P" and "2" indicate Persson and 2MASS, respectively. The SOFI magnitudes have no subscript.

The magnitudes of the stars in the field were then compared with the 2MASS photometry, thus obtaining an "instrumental zeropoint" for the magnitude scale that includes the airmass correction, the mean aperture correction and the actual photometric zeropoint. These zeropoints were then used to cross-calibrate the magnitude scale of the short-exposure images. The "instrumental zeropoints" calculated in this way are summarised in Table 1.

Table 1. Instrumental zeropoints for the long- and short-exposure science frames.

	Band	ZP_{inst} (mag)	rms (mag)
Long exp.	J	22.965	0.099
	H	22.790	0.083
	K_s	22.075	0.088
Short exp. (LF) [2]	J	22.865	0.076
	H	22.747	0.073
	K_s	22.199	0.075
Short exp. (SF) [3]	J	22.798	0.085
	H	22.713	0.099
	K_s	22.183	0.102

The difference in resolution between the 2MASS sample and our own does not significantly influence the calibration as the stars with the largest difference in magnitude, presumably the blended doubles in 2MASS, are rejected from the comparison.

We used the parameters *sharpness* and *chi* given by ALLSTAR to exclude the stars with poor photometry. These parameters measure the roundness of the object and the goodness of the PSF fit and were considered acceptable between –1 and 1 and below 4, respectively. The mean photometric errors after the aforementioned cuts are of 0.03 mag in J, H and K_s for the long exposures and 0.04 mag in the three bands for the short exposures.

The photometry from the long and short exposures were put together to include all the stars from the long exposures (higher signal-to-noise) and those stars from the short exposures that were saturated in the first.

2.2. NACO

J, H, K_s, L' and 4.05 μm near-infrared, high-resolution images of Tr14 cluster core were collected on January 22nd and 23rd, 2005, using the adaptive-optics assisted imager NACO at the Nasmyth-B focus of the ESO/VLT fourth 8-m telescope unit Yepun located at Cerro Paranal, Chile. The NACO (NAOS-CONICA) instrument[4] is equipped with an AO system, NAOS (Rousset et al. 2003), which provides both visible and infrared wavefront sensing and illuminates the CONICA camera (Lenzen et al. 2003; Hartung et al. 2003) equipped with an Aladdin 1024×1024 pixel InSb array detector. The whole system provides diffraction-limited images across the full wavelength range (1–5 μm).

Tr14 was observed in J (1.265 ± 0.25 μm), H (1.66 ± 0.33 μm) and Ks (2.18 ± 0.35 μm) broad-band filters using NAOS visible wavefront sensor and the visible dichroic, indicated for a crowded field with bright stars. The L' (3.80 ± 0.62 μm) and 4.05 μm (4.051 ± 0.02 μm) images were acquired with IR wavefront sensing and *JHK* dichroic suitable for thermal-IR observations. The largest FOV cameras with $56'' \times 56''$ were used, S54 for short-wavelength (1–2.5 μm) observations (54.3 mas/pixel) and L54 (54.7 mas/pixel) for the 4.05 μm narrow-band images. The L' images were collected with the only possible camera, L27 ($28'' \times 28''$, 27.12 mas/pix), which provided fully sampled images according to the Nyquist sampling criterion. The brightest star in the field, HD 93129A ($10^h43^m57^s$, $-59°32'51''$, J2000.0), served as the NGS (natural guide star). On-source and on-sky images were alternatively acquired following an ABBA pattern, where the sky exposures were at a constant distance of 300 arcsec and randomly distributed on a circle surrounding the initial telescope position. The "object" positions were observed with the AO loop closed, while the "sky" positions were observed in open AO loop. The on-source exposures were randomly distributed around the telescope initial position, within a $20'' \times 20''$ Jitter Box. Each of the 6 JK_s and 10 H "object" frames resulted from the mean of 200 sub-integrations of 0.345 s, giving a total exposure time on source of 6.9 min, for the J and K_s images and 11.5 min for the H image. A total exposure time of 9.5 min was obtained for the L' image from 19 frames of 150 sub-integrations of 0.2 s. The narrow-band 4.05 μm image is the result of 10 frames of 70 sub-integrations of 0.4 s giving a total exposure time of 4.67 min. On the night of January 22 the seeing was 0.97, 0.85 and 1.39 at the start of the J, H and K_s observations, respectively. There is no seeing data available for the night of January 23, 2005. Since Tr14 images were collected as part of a backup plan, there was no defined observational strategy and, due to the little time left, no standard stars were observed . For the same reason, no skyflats were collected for the 4.05 μm observations with the L54 camera.

2.2.1. Data reduction

Standard reduction procedures were applied using IRAF and the NACO pipeline[5] (called conicap), which is based on the ECLIPSE[6] library. The raw images were dark-subtracted and flatfielded using the conicap result products. For the JHK_s data, a median sky frame was computed from the best raw sky frames, i.e., the ones with no stars in the field, and subtracted to the dark, flat-fielded images. They were then corrected for hot pixels, cross-correlated and aligned by sub-pixel shifting and combined to produce the final images, while eliminating cosmic rays and other artifacts not removed in the previous processing (for bright objects, a number of electronic and optical ghosts become apparent). For the L' data, each "sky" image was subtracted from the "object" image on a frame-by-frame basis. These pairs were combined, clipping for object pixels, to create an image of an optical ghost, a large circular ring resulting from the subtraction of AO closed loop- and open-loop observations. This "ghost" image was then subtracted from the created pairs, and ghost-subtracted images were aligned and median combined into the final processed L' image. The 4.05 μm data were reduced in a similar way to the L' data but skipping the flat-field due to missing the appropriate skyflat images.

The offsets between the sub-frames were determined with JITTER. The final J, H, K_s, and L' frames were then registered to one another and trimmed at the common area. After the trimming, the final area of the images for photometry was $22''.8 \times 22''.9$. The 4.05 μm image was not used in photometry but served as a cross-reference for the interesting objects found in the L' image (see Sect. 3.10).

Figure 2 shows the image of the centre of the cluster in the H band in logarithmic intensity scale. Both the NACO's characteristic high resolution and the effect of the anisoplanatism are clearly visible in this image.

[4] http://www.eso.org/instruments/naco/

[5] http://www.eso.org/projects/aot/eclipse/conica/

[6] ECLIPSE is a reduction package developed by the European Southern Observatory (ESO), http://www.eso.org/projects/aot/eclipse/

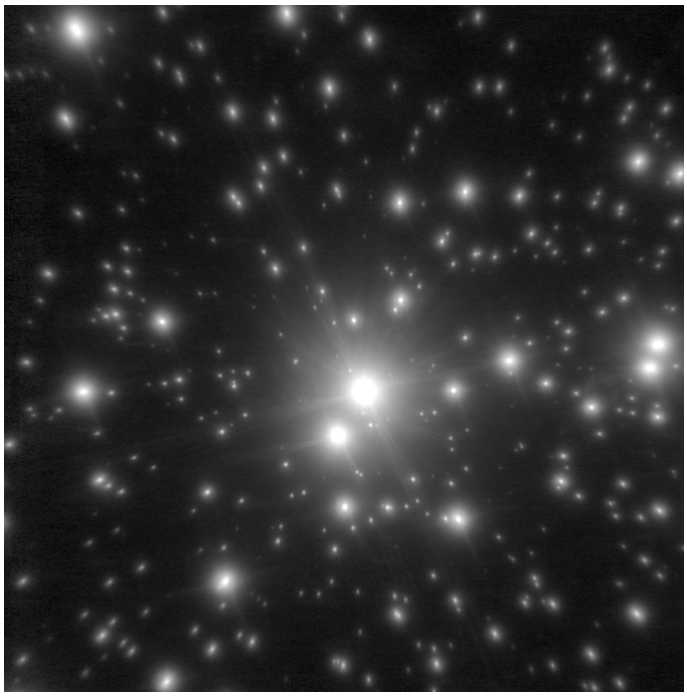

Fig. 2. NACO H band image of the central area of Tr14. The intensity scale is logarithmic. North is up and east is to the left.

2.2.2. Source extraction and photometry

The data suffers from a moderate but significant degree of anisoplanatism, a common effect in observations from adaptive optics. Nevertheless, since we do not have a specific tool to handle this kind of data, we chose to adopt a standard source detection and photometry procedure.

We used IRAF DAOFIND to detect the sources with *FWHM* of 0.″12 to 0.″14 and brighter than 5 times the mean noise in the "clean" areas. We performed PSF photometry with IRAF DAOPHOT using a second-order variable PSF to minimise the effects of the anisoplanatism. The stars used to define the PSF were chosen to be moderately bright, isolated, as much as possible, and spread across the whole extent of the image, which amounted to 15 to 24 stars depending on the frame. The best fits were always obtained for Penny functions, composed of a Gaussian core and Lorentzian wings. The residuals from the PSF subtraction were significant and in particular larger than for the SOFI data due to the anisoplanatism, but overall the same order of magnitude for all objects in each frame.

NACO user's manual does not provide the transformation equations for any standard photometric system. Assuming that there is little difference between NACO and 2MASS systems as is the case for the SOFI data, we have used these data to cross-calibrate the JHK_s data by determining zeropoints to the magnitude scales using the stars common to the both images (see Table 2), thus roughly obtaining the magnitudes in the 2MASS system. This zeropoint includes the correction for all additive phenomena affecting the data so far, namely the airmass correction, the actual photometric zeropoint, and an "aperture correction" that minimises the impact of the large residuals from the PSF fit in the photometry. As noted earlier, the very brightest stars have, in general, brighter residuals which means that the global (zeropoint) correction applied to each frame is probably not enough to yield accurate photometry for these objects. We did not address this problem in detail, so we note that the photometry of these objects from the NACO sample should be interpreted with caution.

Table 2. Instrumental zeropoints for NACO with respect to SOFI.

Band	ZP_{inst} (mag)	rms (mag)
J	23.234	0.094
H	23.540	0.077
K_s	21.737	0.107

The large rms reflect the difference in resolution in an area as crowded as the central part of the cluster. Despite these errors and the ones eventually introduced by the deficient PSF photometry, this calibration appears to be reasonable since the diagrams are perfectly consistent with the data from SOFI (see Fig. 11).

The L' band was not accurately calibrated as we did not have regular standards or catalog information for this band. However, we did estimate a rough zeropoint of 21.2 mag using the overall distribution of points in the $(J - H) - (K_s - L')$ colour–colour diagram by forcing it to be consistent with the distribution in the JHK_s colour–colour plot. The exact calibration of this band is not crucial for our analysis.

Again, we used the parameters *sharpness* and *chi* given by ALLSTAR to exclude the stars with poor photometry. These parameters measure the roundness of the object and the goodness of the PSF fit and were considered acceptable between –1 and 1 and below 4, respectively. The mean photometric errors after the aforementioned cuts are 0.05 mag for J, 0.03 mag for H and 0.04 for K_s and L'.

2.3. Completeness limits

The completeness limits were determined for the long exposures by adding artificial stars of increasing magnitudes to the original frames. For each (0.5 mag) magnitude bin, the stars were added in fixed positions separated from the adjacent ones by two PSF radii + 1 pixels (PSF radius ∼10 pixels) according to the model PSF used for the photometry, thus comprising a grid with the maximum possible number of stars that does not add to the crowding effect. Our 90% completeness limits are therefore $J = 15.88$ mag, $H = 15.00$ mag and $K = 14.52$ mag. The reason for these high completeness limits is the high surface density of sources, leading to blending and some confusion (see next section).

The limits determined above are an average over the long-exposure frames and are not representative of the central, more crowded regions of the images, where the source detection is severely hampered by crowding effects. We have compared the detections in the SOFI (long and short exposures) and NACO samples to have a feel for the completeness in the cluster core and found that only 37, 31 and 38% of the stars detected with NACO are detected with SOFI in J, H and K_s, respectively. This is merely a consequence of resolution: SOFI's resolution element for the current seeing is 1.″4, which is considerable in crowded regions such as the core of massive clusters and, in particular, of Tr14. NACO's resolution element is ten times smaller (0.″14), making it much more adequate when studying these regions. This illustrates well the limitations of seeing-limited photometry in crowded regions. The sensitivity limits, however, are fainter with SOFI for this specific settings: the faintest star detected with NACO is $K_s = 18.6$ mag, whereas the faintest detected with SOFI is $K_s = 19.8$ mag, more than one magnitude fainter.

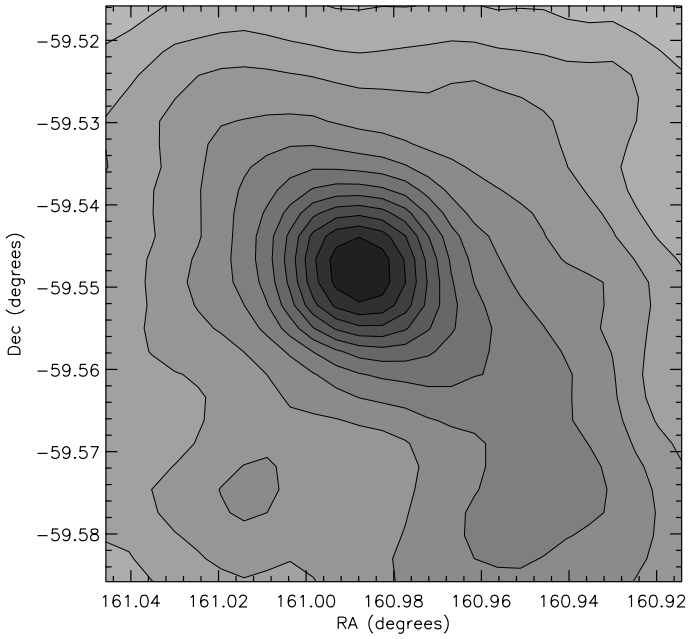

Fig. 3. K_s-band contour plot of the stellar density distribution from the SOFI and NACO data. The highest and lowest density contours correspond to 2330 and 330 sources/arcmin^2, respectively.

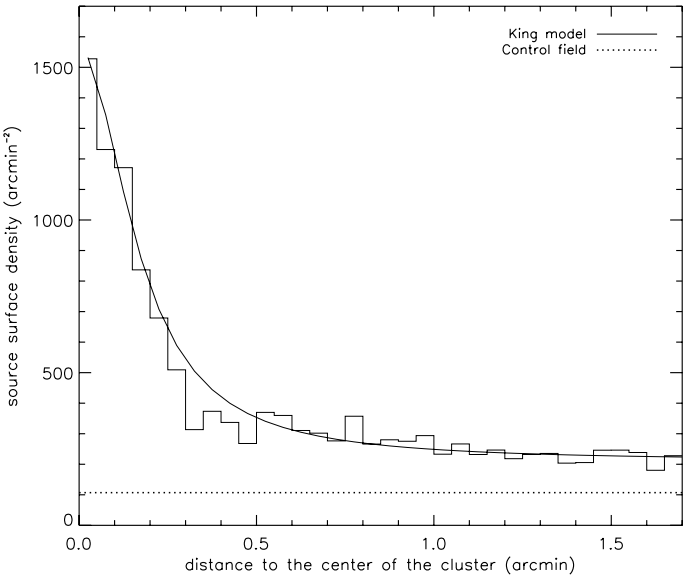

Fig. 4. K_s-band radial stellar density distribution from the SOFI and NACO data. The *solid line* is our best fit to a King (1962) profile.

2.4. Astrometry

The world coordinates for the images were calculated by comparing the positions of some isolated stars with stars in 2MASS. The routines CCMAP and CCSETWCS in IRAF calculated the transformation parameters and applied the transformations to within 0.03″ (1-σ).

3. Results

In the present survey, we detect 3519, 4012, and 4667 sources in J, H and K_s, respectively with SOFI (NTT) and 133, 184, 178, and 72 sources in J, H, K_s and L' with NACO (VLT).

3.1. Spatial distribution

Figure 1 reveals a rich field toward Tr14 and an obvious concentration of stars toward the centre, although not as compact as other massive clusters (e.g., Ascenso et al. 2007). Figure 3 shows the stellar-density contour plot as derived from the K_s-band data from SOFI and NACO. The star counts were obtained by subdividing the region into a rectilinear grid of overlapping squares, counting the number of stars in each square and dividing by the area of the square. The squares were 12″ × 12″ in size and were separated by 6″, the Nyquist spatial sampling interval. The lowest and highest contours correspond to densities of 330 and 2330 sources/arcmin^2, respectively. The distribution is centrally concentrated and elongated toward the SW direction, as already observed by Tapia et al. (2003). The major axis of this elongated shape is roughly perpendicular to the direction of Trumpler 16, a geometry that may be relevant in a scenario of triggered star formation.

The surface density radial distribution of the sources in K_s is shown in Fig. 4. Both NACO and SOFI sources are included, and the bin is 3″ wide. The distribution falls rapidly as we move away from the centre until it becomes roughly constant at a value close to 200 sources/arcmin^2. The *dotted line* represents the mean surface density in the K_s band of our control field and the *solid line* represents our best fit of a King (1962) profile. For this profile we have adopted the equation for the central and concentrated regions where the tidal radius can be neglected, and considered an additive constant C:

$$f(r) = \frac{f_0}{1 + (r/rc)^2} + C. \quad (8)$$

In this notation f is the surface number density at radius r, f_0 is the surface density at zero radius and r_c is the core radius. This function provides a surprisingly good fit to the data considering it should map the density distribution of a single-mass population in dynamical equilibrium (Hillenbrand & Hartmann 1998; Binney & Tremaine 1987), which is obviously not the case for Tr14 or other clusters, as they contain stars over the whole spectrum of masses. The issue of dynamical equilibrium, however, is not as clean cut. On one hand, the cluster has a detectable extension to the SW (see Fig. 3), hence it is not spherically symmetric, and the analysis of Vazquez et al. (1996) suggest it is not yet dynamically relaxed. On the other hand, the calculations of Penny et al. (1993) conclude that it is, although their results are based on a very limited number of sources. Regardless of the physical implications, the core of Tr14 can be robustly fit with a King profile that yields a core radius of 0.′17 (0.14 pc at the adopted distance of 2.8 kpc), a surface density at zero radius of 2.0×10^3 sources/pc^2, and a constant C of 310 sources/pc^2 (210 sources/arcmin^2).

Applying the relation between surface and volume number density of Hillenbrand & Hartmann (1998) for high density environments:

$$n_c = \frac{f_0}{2r_c}, \quad (9)$$

where n_c is the volume density in the centre and f_0 is the surface density in the centre, we obtain a central volume density of 7.3×10^3 sources/pc^3 (2.7×10^3 $M_\odot$ pc^{-3}). This is a small number when compared to the values in the literature[7],

[7] We used Eq. (9) to determine the central volume density whenever the authors provide only the core radius and central surface density.

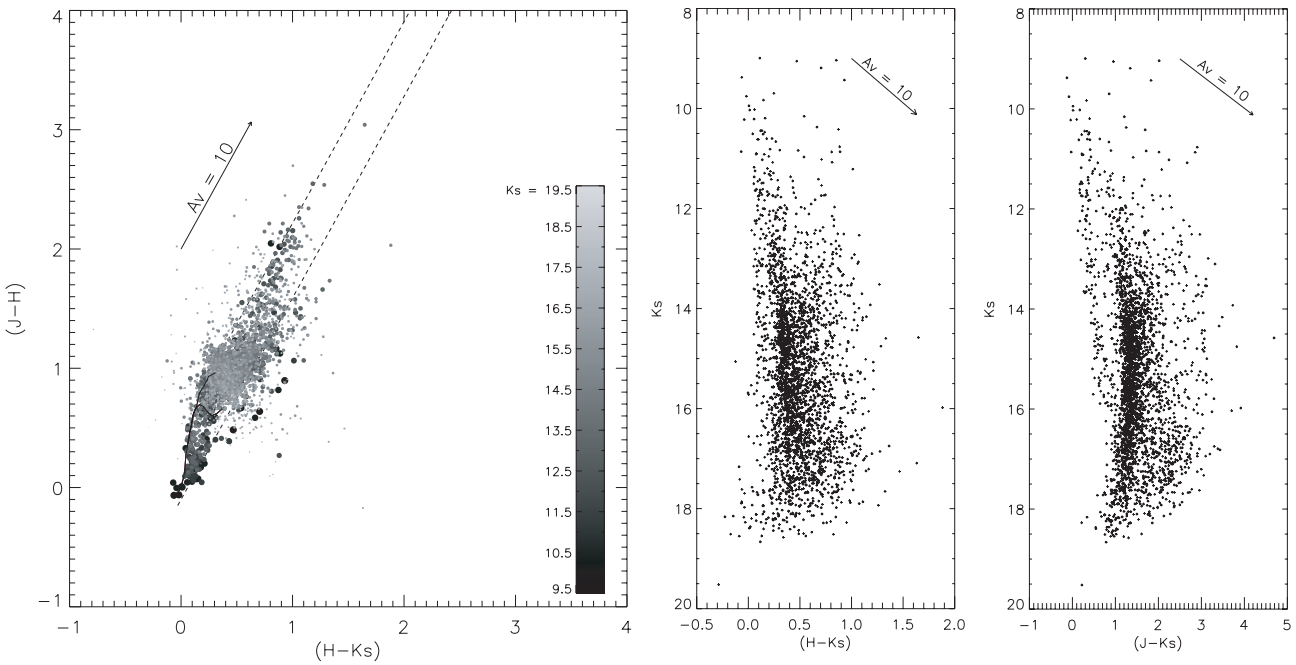

Fig. 5. *Left panel*: $(J - H)$ vs. $(H - K_s)$ colour–colour diagram for the SOFI data. The brightest objects have larger symbols and the dashed lines define the reddening band of Rieke & Lebofsky (1985). *Middle panel*: K_s vs. $(H - K_s)$ colour–magnitude diagram for the SOFI data. *Right panel*: K_s vs. $(J - K_s)$ colour–magnitude diagram for the SOFI data.

both for clusters with a comparable number of O stars such as NGC 3603 or Arches (10^5 and 3×10^5 $M_\odot\,\mathrm{pc}^{-3}$, respectively, Stolte et al. 2006) and for smaller, lower mass clusters such as Orion (4×10^4 $M_\odot\,\mathrm{pc}^{-3}$, Hillenbrand & Hartmann 1998). The implications of this low central density and the fact that the O stars are not only limited to the cluster core, as well as the morphology, dynamical state, and star formation history of the cluster should be addressed further. Since the central density is largely constrained by the NACO data, where we are reasonably complete, it is not likely to be affected by any particular bias. Our core radius for Tr14 compares well with that of other clusters such as Orion, NGC 3603 or the Arches (Hillenbrand & Hartmann 1998; Stolte et al. 2006) but is larger than the core radius of NGC 2316, RCW 36, NGC 3606, or R 136 (Teixeira et al. 2004; Baba et al. 2004; Sung & Bessell 2004; Stolte et al. 2006).

The fit of the King function without the constant C is poor and fails to adjust the tail of the distribution in Fig. 4. However, its value is twice as high as the contamination derived from the K_s band of the control field (107 sources/arcmin^2), suggesting the presence of a significant extended population in the area of the cluster, be it composed of objects belonging to either the cluster or the complex, or of sources unrelated to the star forming region, in the latter case implying that the real contamination of the science field is twice as high with respect to the control field. The nature of these sources and the overall contamination level will be addressed further in Sect. 3.2.

3.2. Foreground population

The average reddening toward the cluster can be estimated through the analysis of colour–magnitude and colour–colour diagrams and the fitting of main sequence (MS) and pre-main sequence (PMS) models to the data. Figure 5 shows the $(J - H)$ vs. $(H - K_s)$ colour–colour diagram (*left panel*, hereafter CC diagram) and the K_s vs. $(H - K_s)$ and K_s vs. $(J - K_s)$ colour–magnitude diagrams (*middle* and *right panels*, hereafter HK CMD and JK CMD respectively) for the SOFI data. The size of the symbols in the CC diagrams maps the brightness of each object in K_s, the brightest objects having the largest symbols.

None of the diagrams shows an obvious foreground population, i.e., a population that is clearly separated from the cluster population by an "extinction wall" eventually produced by the embedding molecular cloud that should be surrounding the cluster, also in the foreground. If we look closely, however, we can see that the brightest stars in the CC diagram appear to be marginally separated in two distinct sequences, a "blue" sequence at lower reddening and a "red" sequence at slightly higher reddening. If we identify the two sequences by eye as depicted in the *left panel* of Fig. 6[8], we can see that they present different spatial distributions, the blue sources appearing uniformly distributed across the field, while the red sources follow the density contour distribution toward SW (Fig. 7). Furthermore, the red sequence is composed of systematically brighter stars (0.5 mag brighter on average), indicating some kind of intrinsic difference (age?).

It is clear from the comparison with the MS locus that both tentative sequences are composed of MS objects. The overplotted lines in Fig. 6 represent the empiric MS of Bessell & Brett (1988) in the CC diagram and of Lejeune & Schaerer (2001) in both CMDs, reddened by $A_v = 0.5$, 1.4 and 2.6 mag. The blue sequence is compatible with an extinction between 0.5 and 1.4 mag in the CC diagram and the HK CMD, although the latter favours the higher values. The red sequence is fit well by an extinction of 2.6 mag in both diagrams. Oddly enough, there is no clear separation of the two sequences in the JK CMD. The unique sequence in this diagram is adjusted best by the MS at $A_v = 2.6$ mag, although still marginally compatible with the 1.4 mag reddening found for the other diagrams. The vertical

[8] Since the two sequences are defined by eye, there is likely some degree of cross-contamination between the two samples. These criteria are therefore not good membership indicators for the individual objects.

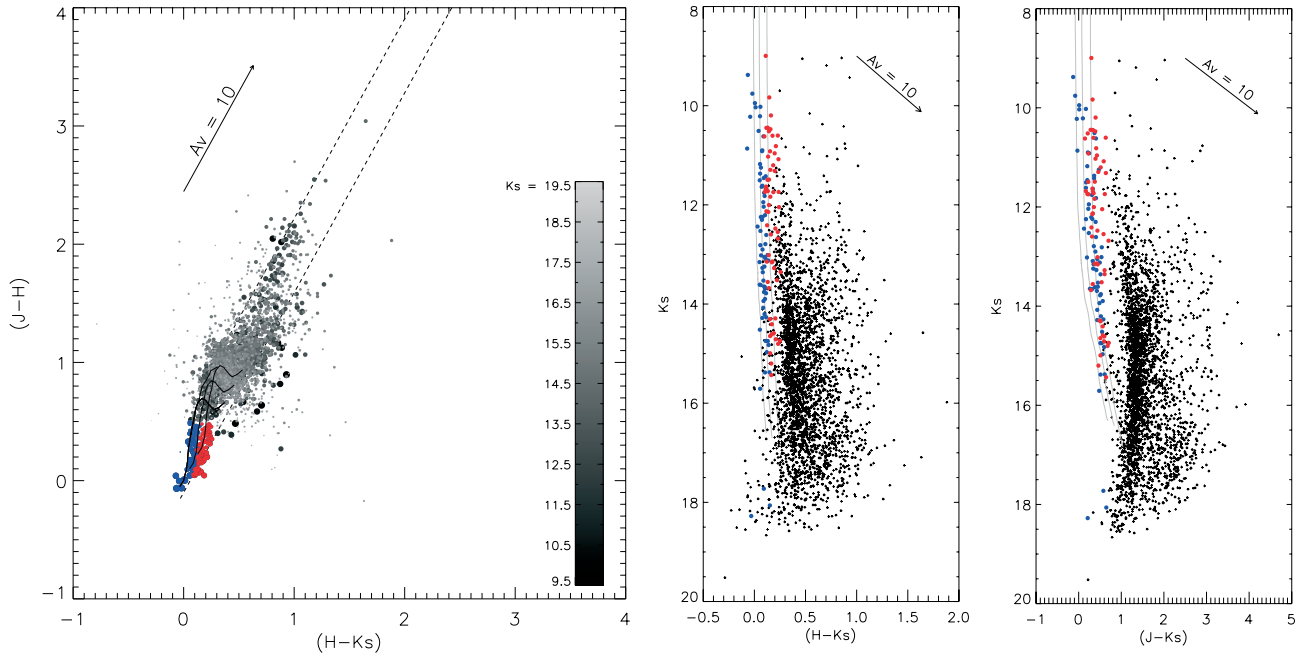

Fig. 6. Same as Fig. 5 but with the main sequence of Bessell & Brett (1988) (*left panel*) and of Lejeune & Schaerer (2001) (*middle* and *right panels*) reddened by A_v = 0.5, 1.4, and 2.6 mag.

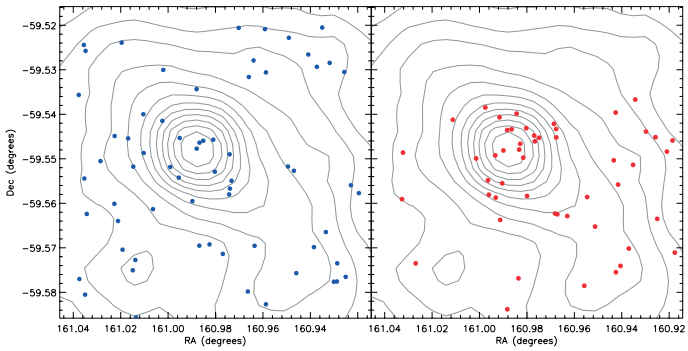

Fig. 7. Spatial distribution of the sources in the blue and red sequences (*blue circles* and *red circles*, see text). The light contours are the same as in Fig. 3 (surface density contour distribution).

sequence around $(J - K_s) \sim 1.3$ mag represents the PMS population of the cluster and is consistent with $A_v = 2.6$ mag when adjusted by the models of Palla & Stahler (1993), the same value found before for the red sequence, suggesting association with the cluster. The presence of a MS population in a young cluster is not necessarily odd: the brightest end should reflect the MS nature of the most massive cluster members, whereas the faintest end can be explained if the cluster has undergone continuous or several episodes of star formation, or by contamination from older stars formed in the Carina complex. We therefore assume a value of $A_v = 2.6 \pm 0.3$ mag for the global reddening toward the cluster and assume that the red sequence is physically associated to the cluster.

Regarding the origin of the stars in the blue sequence, it may be useful to consider the Carina Nebula as a global, dynamic, and interacting system. The smaller extinction found for this sequence locates its components in the foreground of Tr14, although they are unlikely to be regular field stars, foreground to the whole Carina complex, but more evolved members of the other nearby clusters in the nebula that have had time to spread as far as the location of Tr14. This is because 1) the sequence is well-defined, hence the sources should be at about the same distance, and 2) the sequence contains massive OB stars, not easily found in the field.

A scenario of dynamical redistribution of the sources in the complex is not improbable given the amount of different clusters with massive stellar content associated to the cloud. In previous studies, Feinstein et al. (1973) have proposed that Tr14, Tr16 (to the south) and Cr232 (to the northeast) belong to the same group and were supported by the proper motion studies of Cudworth et al. (1993), who also conclude that the three are physically associated. In 1976, Feinstein et al. suggested that Cr228 had stars from Tr14/Tr16, despite this cluster being located 10′ south of η Car. Recently, Tapia et al. (2003) reported the lack of a significant low-mass population in Cr232 suggesting in this way that it was not a cluster. Did the cloud not form the low-mass population to go with the O and B stars that characterise Cr232 or has this population been ejected away from the core by some dynamical process? All the nearby clusters are thought to be older than Tr14, which is consistent with the MS nature of the objects in the sequence. Furthermore, their tight distribution in A_v also suggests a tight spatial constraint for their location, as expected if they were somehow associated to the nebula. All these possibilities make it plausible for the observed blue sequence to have originated in one or several of these groups. The fact that they are uniformly distributed across our field (Fig. 7) does not favour any particular origin.

We would like to note that, although the separation of the MS stars into two distinct sequences does appear real, the limits are too faint to exclude the possibility of a single population with a gradient of extinction. The remaining analysis of these data is not significantly affected by either scenario.

3.3. Cluster structure: a well-defined core-halo structure

We now re-address the foreground/background contamination issue already introduced in Sect. 3.1, as well as the nature of the additional uniform population found then in the radial

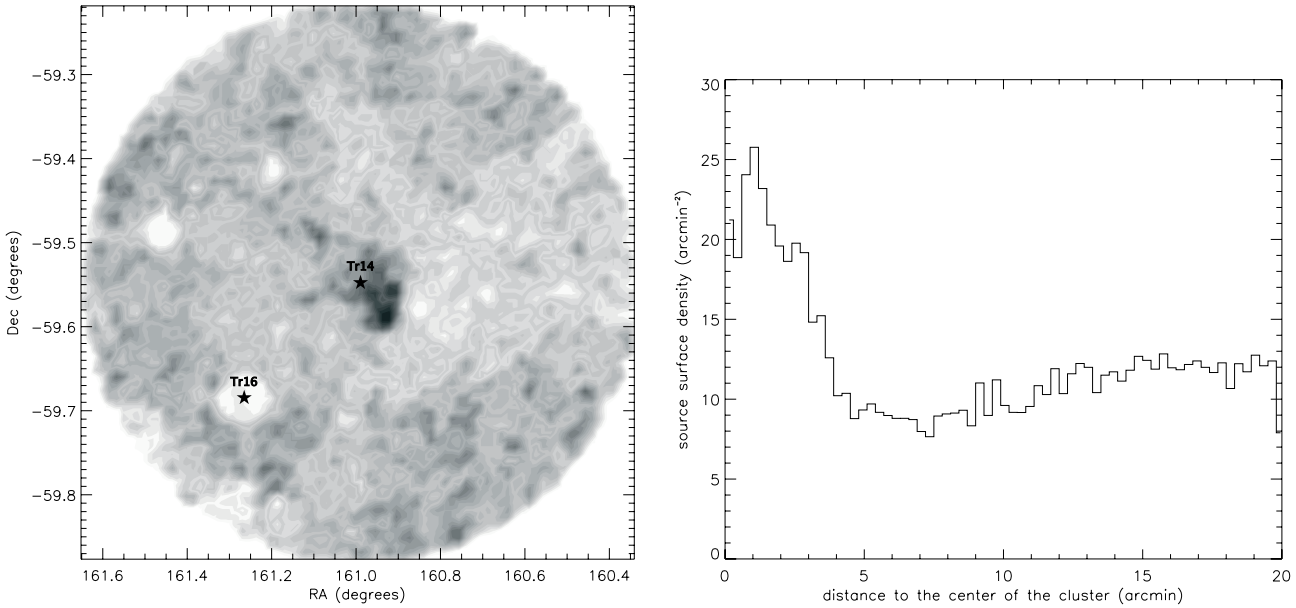

Fig. 8. *Left panel*: 2MASS stellar density map in the area containing and surrounding Tr14. The darkest areas correspond to the highest densities. The locations of Tr14 and Tr16 (namely η Car) are indicated with a star and the appropriate indication. *Right panel*: radial density profile for the same 2MASS data. The bins are 12″ wide.

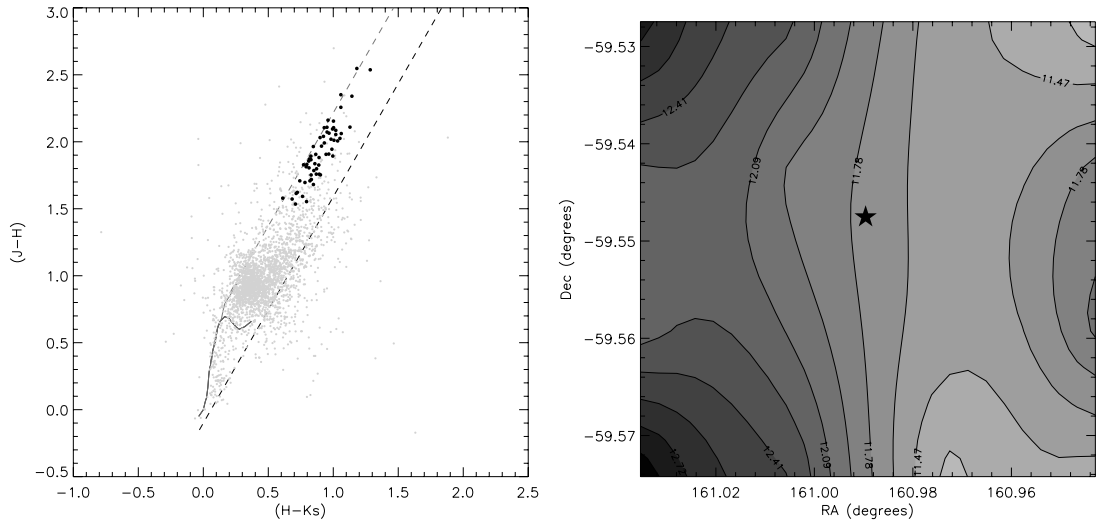

Fig. 9. *Left panel*: $(J - H)$ vs. $(H - K_s)$ colour–colour diagram for the cluster, highlighting the sources used to build the extinction map as *black filled circles*. *Right panel*: background extinction map for the central area of our field. The darker contours are for higher extinctions, and the *star symbol* represents the position of the O2.

surface density profile. Let us now consider only the sources detected in all three J, H and K_s bands, as opposed to including all sources detected in K_s. The radial profile of the cluster becomes a scaled-down version of the one on Fig. 4, flattening around the same radius at a density of 150 sources/arcmin^2 (2226 sources for the science-field area), and the control field mean density drops to 26 sources/arcmin^2 (which translates to a total of 386 contaminant sources for the science field area). For comparison, we detect a total 2808 sources in J, H and K_s in the science field. If the control field was to be a good representation of the foreground/background contamination, then the science field should contain about 386 sources unrelated to the cluster. However, we detect only 130 stars in the well-defined main-sequence of the CMDs, half of which belong to the red sequence defined above, which we believe to be part of the cluster. As a result, we can account for only about 65 of the inferred 386 contaminant sources, unless the remaining contamination is caused by background in the form of highly reddened stars hidden in the PMS region of these diagrams. This seems very unlikely since the control field significantly overestimates the contamination of the science field. Indeed, the scarcity of foreground field stars seen in the CMD diagram, suggests that the Carina Nebula is located in the first plane of the Sagittarius-Carina (S-C) spiral arm, where one expects little contamination from the local arm and also little or none from the S-C arm itself. Because, contrary to the cluster field, it does not have a giant molecular cloud to block the background (Tapia et al. 2003), the control field could be probing deeper into the S-C arm, hence containing a relatively larger number of field sources.

Even if we do (over)subtract the mean control field density from the cluster's density profile as a rough measure of the contamination, we will still have to explain a stellar surface density of ∼125 sources/arcmin^2 (which translates into 1870 sources for the science field area, or 70% of the total number of stars in the JHK_s sample) present in the field in the form of an extended population. Since the level of contamination from the control field more than accounts for the totality of our main-sequence stars, we can only conclude, based on the CMD diagrams, that this extended population is largely composed of PMS objects and for this reason must be associated with the cluster or with the larger-scale Carina complex. If this is the case then the cluster core, as characterised by the King profile in Fig. 4, must be embedded in an extended halo of young stars. In favour of this argument, recent X-ray studies of this region (Sanchawala et al. 2007) have found the presence of an extended population of X-ray emitters, likely late-type PMS stars, surrounding the Tr14 cluster core (see Fig. 12). Bate et al. (2003) present results of a 3D simulation that follows the collapse and fragmentation of a large-scale turbulent molecular cloud to form a stellar cluster. They concluded that young stars can still travel significantly away from their birthplace in a typical star formation timescale, creating a halo surrounding the core of the cluster. They do not characterise their halo, since their cluster only has 50 objects, but a similar mechanism could be at the origin of the massive halo observed in Tr14. We can speculate further that the ratio of stars in the halo is likely to be a function of the initial distribution of molecular gas, which would vary from cluster to cluster.

In the left panel of Fig. 8, we present a 0.35° 2MASS K-band stellar density map centred on Tr14. Although 2MASS does not have the spatial resolution to account for the peak in stellar density at the core of Tr14, it is obvious that there is an extended and isolated stellar population in excess of the average stellar density in the map, on which the Tr14 core is embedded. It seems that Tr14 has a well-defined core-halo structure, where, and for the area surveyed, we have about 30% of the cluster residing in the King-like core and the rest (70%) in the extended halo. Given that we do not survey the entire halo, the true ratio between the core and halo population should be more extreme. To characterise the size of the halo population we present in Fig. 8 (right panel) the radial profile of the stellar surface density, centred on Tr14. The dip between 0 and 1 arcmin is caused by the crowded core (see Fig. 4) which is not resolved in the 2MASS data. We conclude from this profile that the average radius of the halo population is about 5 arcmin. The shallow dip between 5 and 10 arcmin is very likely due to the heavy extinction regions surrounding Tr14. The peak of the halo population is located in the well-known photodissociation region (left panel of Fig. 8) where star formation is currently very active (Brooks et al. 2001; Rathborne et al. 2002; Tapia et al. 2003, 2006). This region is just outside our survey and so a similarly deep and high-resolution, but wider coverage, study will characterise the nature of the entire halo region better.

3.4. Background extinction

We can estimate the spatial distribution of background extinction in the cluster area through NIR colour excesses (Lada et al. 1994; Alves et al. 1998) of the (SOFI) sources most likely to belong to the background. This selection comprises all the sources brighter than $K_s = 15.5$ mag and with $(J - H) > 1.5$ mag (*left panel* of Fig. 9) and amounts to a total of 60 stars. The $(H - K_s)$ colour of each object was transformed into individual visual extinctions A_v by assuming an intrinsic colour of $(H - K_s)_{int} = 0.15$ mag for these stars (mean colour for the giants) and the reddening law of Rieke & Lebofsky (1985):

$$A_v = 15.87[(H - K_s)_{obs} - (H - K_s)_{int}]. \quad (10)$$

The extinction map (*right panel* of Fig. 9) was then obtained by dividing the field into overlapping pixels of 112″ side separated from one another by half a pixel and averaging the individual extinction of all objects falling on each pixel. The large pixel size reflects the need to guarantee acceptable statistics in each pixel, given the small total number of stars available for the map.

The extinction map reveals a clear gradient in the east-west direction with the largest extinction to the east, although the variations in A_v around the mean value are small ($\langle A_v \rangle = 11.95$ mag, $\sigma = 0.53$ mag). This implies that the cluster is located towards the near-face of the molecular cloud as seen from Earth, since the total foreground extinction is 2.6 A_V mag. The bright stars in the centre of the cluster are almost aligned horizontally to the west of the O2 star HD 93129A (*star symbol* in Fig. 9) as can be seen in the three colour image of the cluster (Fig. 1), suggesting a correlation between the extinction gradient and their impact on the cloud. Also, this map correlates well with the CO large scale map of Brooks et al. (2003), where Trumpler 14 seems to be located in a "valley" of CO emission, at the edge of the Northern Molecular Cloud.

The total molecular gas traced by this extinction map can be derived from the extinction map using the following simple relation:

$$M = d^2 \mu \beta_K \int_\omega A_K \, \mathrm{d}^2\theta \quad (11)$$

where d the distance to the cloud, μ the mean molecular weight corrected for helium abundance, $\beta_K \simeq 1.67 \times 10^{22}$ cm^{-2} mag^{-1} is the ratio $N(H_I) + N(H_2)/A_K$ (Savage & Mathis 1979), and the integral is evaluated over the whole field ω. Assuming a standard cloud composition (63% hydrogen, 36% helium, and 1% dust), we find $\mu = 1.37$ and a total mass $M \sim 2500\ M_\odot$, where the uncertainty is dominated by the distance uncertainty to this region.

3.5. Distance

Assuming the stars in the red (main) sequence are cluster members or are, at least, at the same distance and reddening as the cluster, we can try to constrain the distance by fitting of MS tracks. The possible fits of the MS of Lejeune & Schaerer (2001) to the data allow for distances between 2.1 and 3 kpc, well within the range found in the literature. Since we cannot constrain the distance any further with our data we, adopt the distance of 2.8 kpc derived by Tapia et al. (2003) for Tr14 from spectral parallax in the optical and NIR of 17 (cluster) stars.

3.6. Excess fraction

Figure 10 shows the distribution of sources in the $(J-H)$ vs. $(H-K_s)$ (SOFI data, *left panel*) and $(J-H)$ vs. (K_s-L') (NACO data, *right panel*) colour–colour diagrams. Both diagrams present a fraction of stars to the right of the reddening band suggesting the presence of sources with intrinsic near-IR excess emission from circumstellar envelopes and/or disks. The fraction, f_{exc}, of sources with NIR excess emission was defined, as usual, in the following way:

$$f_{exc} = \frac{N_{exc}}{N_{cl}}, \quad (12)$$

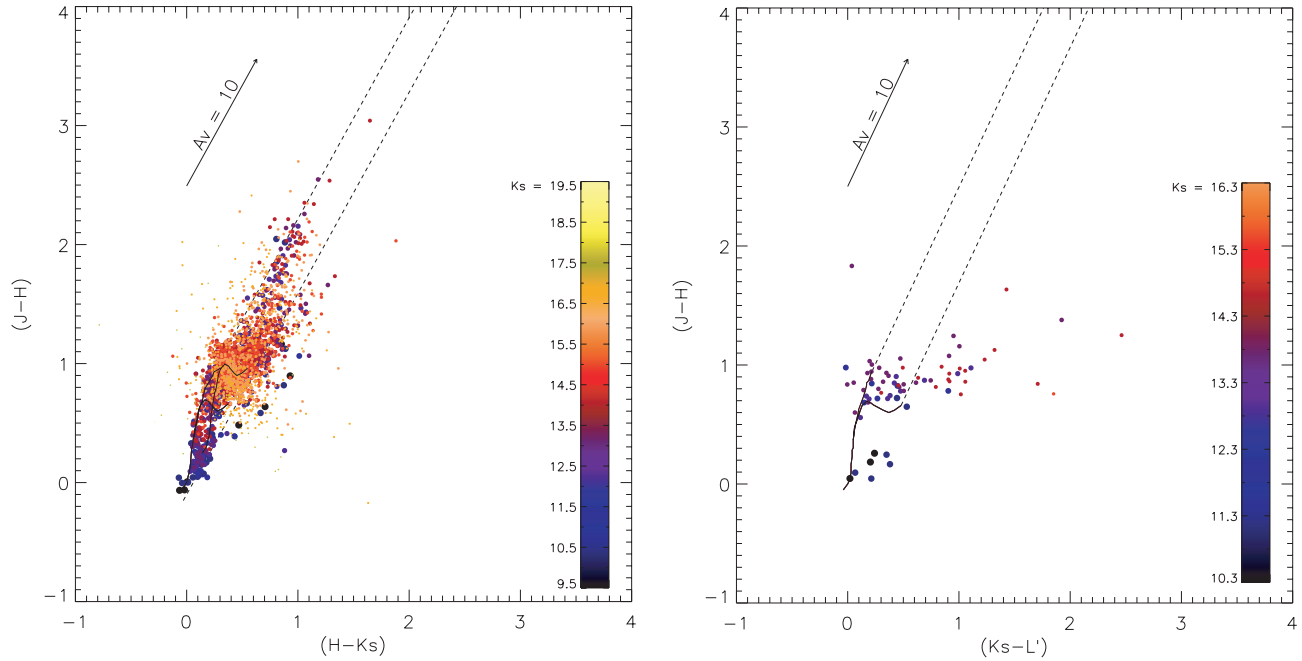

Fig. 10. *Left panel*: $(J-H)-(H-K_s)$ colour–colour diagram for the SOFI data. The *solid line* on the data represents the main-sequence of Bessell & Brett (1988) reddened by $A_v = 2.6$ mag. *Right panel:* $(J-H)-(K_s-L')$ colour–colour diagram for the NACO data.

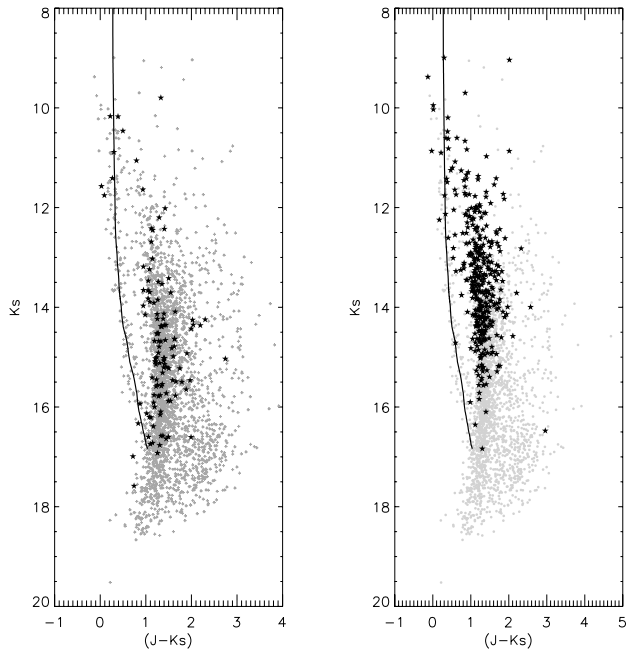

Fig. 11. *Left panel*: K_s vs. $(J-K_s)$ colour–magnitude diagram for the NACO data (*black stars*) superposed on the SOFI data (*gray plus signs*). *Right panel*: location of the sources from ANCHORS detected in X-rays (*black stars*) superposed on the SOFI data (*gray plus signs*) on the K_s vs. $(J-K_s)$ colour–magnitude diagram.

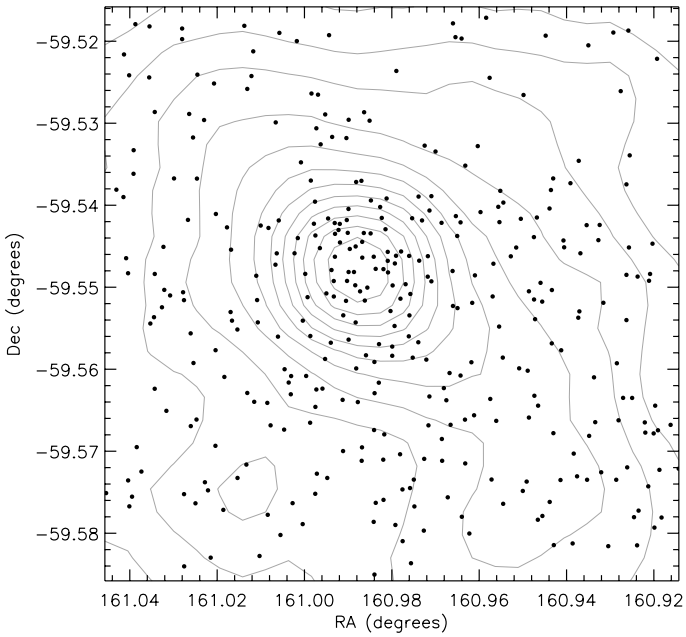

Fig. 12. Spatial distribution of the sources detected with *Chandra* (ANCHORS database). The light contours are the same as in Fig. 3 (surface density contour distribution).

where N_{exc} is the number of sources with excess, i.e., the number of sources that fall to the right of the reddening band subtracted of those that fall to the left of the band to statistically account for the effect of random photometric errors. N_{cl} is an estimate of the number of cluster members – for the SOFI data, it is the total number of sources in the sample subtracted of a constant contamination level to account for the presence of sources foreground and background to the cluster in the field, and for the NACO data is simply the number of sources in the sample since there is no appreciable contamination.

The contamination level for the SOFI data has been taken from the mean density of the control field from the sample common to the three bands, which amounts to 26 sources/arcmin^2 (see Sect. 3.2). Since we believe this to be an overestimate of the actual contamination in the science field, the alternative would be to use the number of stars in the blue sequence described in Sect. 3.2 as the number of "contaminants", but in this way we would not be accounting for the background contamination

that could be significant. Using the control field, we obtain an excess fraction of 5% for the SOFI data. For reference, if we had used the tail of the density distribution as the contamination level for the science field (therefore including what we called the halo stars in the calculation as contaminants), we would obtain a value of 25% for the SOFI excess fraction.

The density of sources with excess follows the global density distribution for the SOFI sample, slightly increasing toward the centre and flattening for larger radii. After subtracting a constant density of 12 sources/arcmin^2 to the excess profile to account for the sources that fall to the left of the reddening band, the tail of the profile goes to zero. Considering that the outer parts of the field are dominated by halo stars this result suggests either a very small and constant, or else absent, fraction of *JHK*excess sources in the halo population, suggesting, perhaps, that the halo population is relatively older on average then the core population, although this is definitely not the case for the southwest end of the halo (see Fig. 8, left panel) where active star formation is currently taking place. More observations are necessary to address the halo excess issue, namely in the excess-sensitive L band.

The excess analysis of the NACO data is somehow more complex. Using the procedure described above, we derived the excess fraction from the JHK_s data for comparison with SOFI and found a value of 34%, almost one order of magnitude higher than that of SOFI. We did expect to find a larger excess fraction in the most concentrated area of the cluster, since (1) this area is dominated by cluster members, whereas the outer areas have a larger contribution from the foreground/background sources; (2) this is where we expect to find the most stars according the spatial distribution of sources (see Sect. 3.1), the low-mass stars being dominant; and (3) this is the area most prone to crowding, therefore most sensitive to incompleteness effects in the low-mass end. However this value is much too different to be explained by these effects alone. In the process of investigating the possible causes for such a large difference, we found a suspicious spatial distribution of the excess sources in the NACO sample. Rather than being uniformly distributed across the field, the NACO excess sources concentrate around the O2 star HD 93129A in a ring. This distribution follows the pattern of the anisoplanatism from the adaptive optics, radially increasing from the guide star, which suggests this excess enhancement is caused by an AO-related effect. Our best guess for the origin of this effect goes back to the calibration of the photometric scale. Under ideal conditions, the anisoplanatism should decrease with increasing wavelength but, in our images, it is worse in H than in J, and in K_s when compared to H. This causes the PSF of the stars farthest from HD 93129A – the guide star used for the AO correction – to be increasingly more elongated in J, H and K_s, thus distributing the flux over an increasingly larger area and causing the brightness of these stars to be increasingly underestimated for longer wavelengths. Since the anisoplanatism affects a large fraction of the stars in the sample, the calculation of the zeropoint must also have been affected by trying to compensate for this effect, causing a "reddening" of the sources that mimic the characteristic colours of the objects with excess. The JHK_s excess fraction derived from the NACO data is therefore overestimated and should not be regarded as accurate. We had hoped that our conservative error cuts in *sharpness* and *chi* (see Sect. 2.2.2) had dealt with the anisoplanatism is such a way as to reject the most elongated sources. That it did not illustrates the limitations of the IRAF PSF fitting routines when faced with adaptive-optics data.

The NACO JHK_sL' data present an excess fraction of 35%. Although the anisoplanatism is barely visible in the L' band, a similar effect to the one described above for J, H and K_s could still be present in this calculation. However, since the spatial distribution of the sources with L'-band excess does not follow the anisoplanatism pattern, we believe this is not the case. The cause for this may be that the centroid of the AO-affected sources in JHK_s is systematically offset from the actual position measured by the anisoplanatism-free L' band, causing the affected sources to be discarded from the common sample and thus eliminating the false excess sources. Furthermore, since the L'-band is considerably more sensitive to excess emission than K_s is, we expect any residual manifestation of this effect to be diluted in the large separation induced by the L' band on a $(J-H)$ vs. (K_s-L') diagram, hence not affecting the result much. The large difference between this excess fraction and that of SOFI is therefore most likely due to the true excess emission rather than to the AO-induced effect. The value from the L' band should anyway be underestimated, given the bright completeness limit in this band and the fact that the faintest stars usually account for the majority of excesses in a cluster (Haisch et al. 2001a; Carpenter et al. 2006). Also, we note that this excess fraction, having been derived only for the cluster core, may not be (and probably is not) representative of the excess fraction in the cluster as a whole.

Perhaps most important is that over 70% of the sources belong to the halo, and are therefore further away from the destructive ionisation fields surrounding the massive OB stars, which seems to imply that the lifetime of circumstellar disks in massive clusters is not simply correlated to the ionising flux from the most massive stars in the cluster. If the fraction of excess sources in Tr14 was to follow the time evolution derived for nearby, although less massive, clusters (Haisch et al. 2001b), one would infer that the cluster core should be about 4 Myr or younger. This age estimate is consistent with the age estimate of this cluster (see next section), although this cluster has on average about two orders of magnitude more ionising flux than the relatively nearby clusters studied in Haisch et al. (2001b).

3.7. Age and age spread

We used PMS isochrone fitting to the data on the JK CMD to derive the age and age spread of the cluster. Like in an HR diagram, the PMS isochrones in a CMD have a descending, vertical component that corresponds to the *Hayashi* tracks, a more horizontal component equivalent to the *Henyey* tracks (just before the beginning of hydrogen burning), and another vertical component located roughly along the ZAMS. Since the low-mass stars, the most abundant in a cluster, spend more time on the *Hayashi* track than on any of the subsequent stages (Stahler & Palla 2005), a young cluster population is expected to exhibit a well-defined vertical sequence merely due to statistics. Furthermore, since the vertical tracks for different masses do not separate well in $(J-K_s)$, this sequence should be relatively thin in the absence of differential reddening. This is indeed observed in most clusters and in Tr14 in particular ($(J-K_s) \sim 1.3$ mag, *right panel* of Fig. 5), despite the actual presence of differential reddening. Although this sequence is too confusing (data) and too ambiguous (models) to allow for reliable isochrone fitting, it is possible to estimate the age of the youngest PMS objects in the cluster simply by tracing the magnitude of the brightest stars in this sequence. For the assumed distance (2.8 kpc), this is consistent with a minimum age between 0 (i.e., the birthline) and 0.3 Myr (Fig. 13), which is compatible with the ages of the most

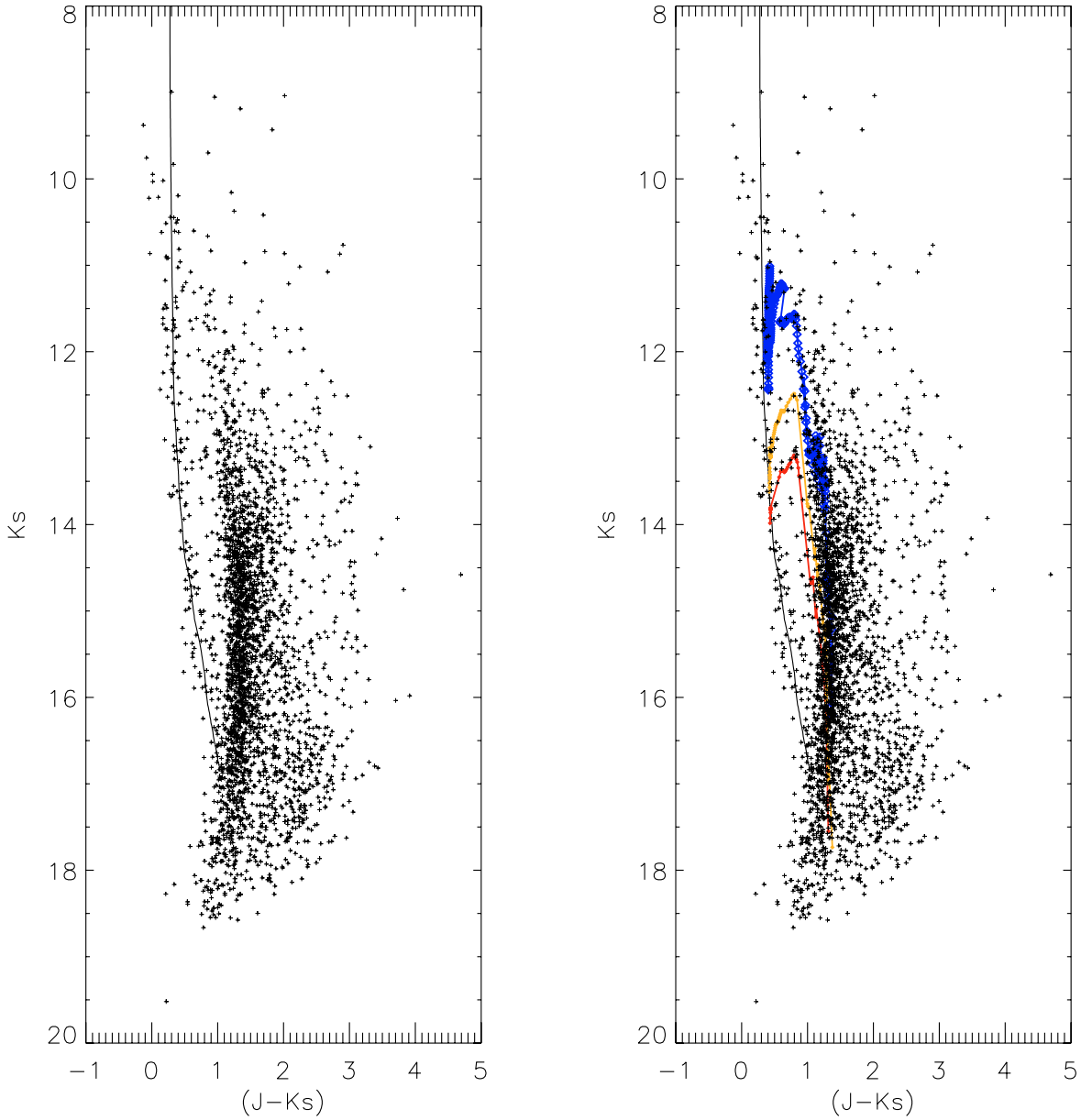

Fig. 13. K_s vs. $(J - K_s)$ colour–magnitude diagram for the SOFI data without(*left panel*) and with (*right panel*) the PMS isochrones of Palla & Stahler (1993): 0.0–0.3 Myr (*blue*), 1.4–2.5 Myr (*orange*), and 3.2–5.0 Myr (*red*).

massive stars. In particular, the sources detected in the X-rays with *Chandra* from the ANCHORS database[9] (Spitzbart & Wolk 2004) (81.1% of which have NIR counterparts) are mostly located in the PMS region of the JK CMD and are consistently distributed along the youngest isochrones, quite similarly to the distribution of the NACO data from the cluster core (Fig. 11). Spatially, these sources do not contradict the surface-density distribution of the cluster, as they appear to concentrate toward the centre and the SW quadrant of the frame (Fig. 12), although there is a significant fraction still scattered in the field.

The horizontal, *Henyey* tracks make up a transition region between the MS and PMS populations that could, in principle, also be used to constrain the age of a cluster. In the case of a coeval population, the data should present a well-defined "arc" in the gap between the PMS and MS vertical sequences, as all the stars in a given mass range would be located in the same well-defined isochrone. This is also valid for several populations within the same sample, in which case this gap would be populated by as many arcs as different (coeval) populations providing the age difference between populations would be large enough to cause a significant separation in the diagram. In the case of Tr14 there are very few objects in this transition region (roughly $0.5 < (J-K_s) < 1$ mag) and no specific horizontal track is particularly well-defined, although there are some small, arc-shaped concentrations that are probably worth exploring. The first and probably most significant is found near $K_s \sim 13.3$ mag, which, at the adopted distance, corresponds to an age between 3.2 and 5 Myr (Fig. 13). Around $K_s \sim 12.7$ mag, there is another small concentration of points well fit by the isochrones of 1.4 to 2.5 Myr and, willingly, there is yet another between $K_s \sim 11$ and

[9] http://cxc.harvard.edu/ANCHORS/

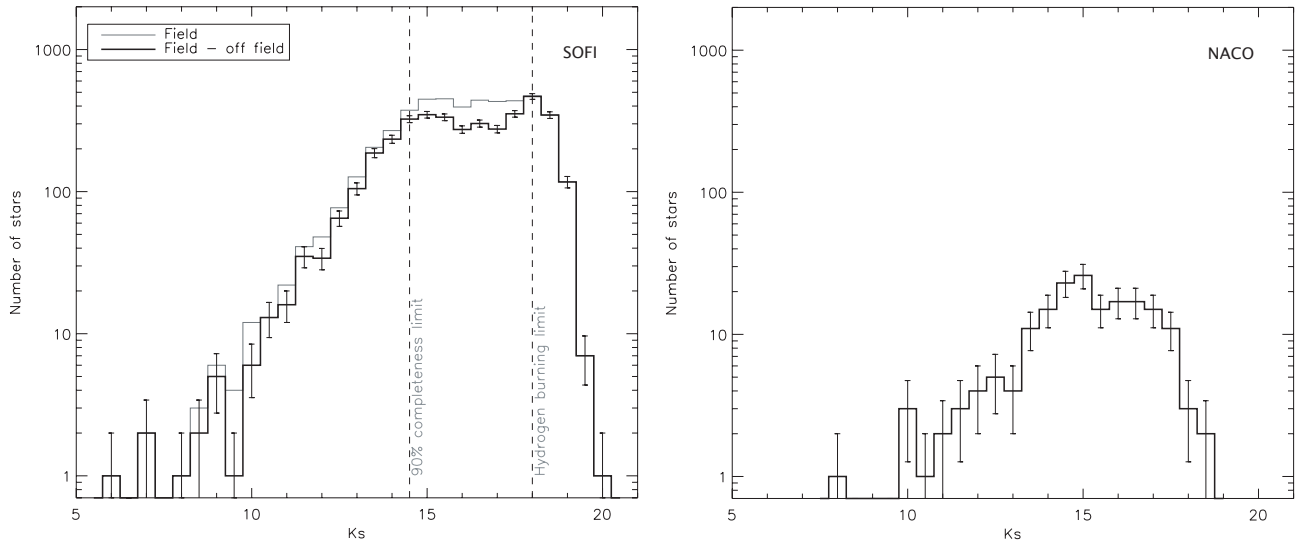

Fig. 14. *Left panel*: K_s-luminosity function for the SOFI data. The *light* and *dark lines* represent the function before and after the control field subtraction, respectively. *Right panel*: K_s-luminosity function for the NACO data. No control field subtraction was applied.

~11.7 mag, well fit by the 0 to 0.3 Myr isochrones. These concentrations are arguably significant and are discussed here only for the sake of completeness in the analysis. If they are real, they may indicate several episodes of star formation that may eventually be related to the history of energetic events in the complex in a scenario of triggered star formation. If, on the other hand, we interpret these enhancements as chance alignments of a random distribution of sources in the PMS-MS transition region, then a continuous star formation scenario that would not favour any of the isochrones in particular would be more appealing. Either way these data suggest the cluster has formed over a long period of time as opposed of having formed in a single and fast episode.

If the red sequence found in Sect. 3.2 does indeed belong to the Carina region then it would represent a population of objects older than 6 Myr, the time it takes most stars to reach the ZAMS. The same argument is valid for the halo population with the exception of the age constraint since it is clear that this population is PMS in nature (see Sect. 3.2). With our data we cannot tell whether these populations eventually originated in Tr14 or anywhere else in the complex.

3.8. K_s- luminosity function

As suggested in Sect. 3.1 the science field is very likely contaminated by foreground/background sources that must be accounted for when building the K_s-luminosity function (KLF). This is done for the SOFI data by statistically subtracting the foreground and background objects estimated by a nearby field at the same galactic latitude as the cluster. Although this field was observed with the same exposure time as the long-exposure science frames with the aim of obtaining a field of the same depth, the weather conditions deteriorated and the control field does not go as deep as the science field. The faintest star in the control field is $K_s = 17.90$ mag, whereas the faintest star in the science field is $K_s = 19.83$ mag, almost two magnitudes fainter.

Since we only observed a control field for the long exposures, we also lack information about the contamination in the range of magnitudes $K_s = 9.2$ mag to 11.3 mag, the saturation limit for the SOFI long exposures. This was overcome by combining the information in the 2MASS data for the control field for the bright objects ($K_s < 14$ mag) and our control field for the faint ($K_s > 14$ mag). As stated before, it is likely that this control-field KLF may be overestimating the actual contamination in the science field since, according to Tapia et al. (2003), the cloud wrapping the cluster should block a significant fraction of the background contamination. We did not estimate a control-field for the NACO data, because it does not appear to have a significant number of non-cluster members judging by the colour–magnitude diagram in the *left panel* of Fig. 11.

Figure 14 shows the KLF for the SOFI data (*left panel*) and the NACO data (*right panel*). The magnitude bins are 0.5 mag wide. The SOFI KLF rises smoothly until $K_s = 14.5$ mag (the 90% completeness limit in this band) and flattens toward fainter magnitudes. The peak around $K_s = 18$ mag is produced by the brighter completeness limit in the control field when compared to that of the science frames, so it is not real. That the KLF does not decrease even after the 90% completeness limit suggests the actual distribution should continue to rise for fainter magnitudes.

3.9. Cluster mass

With the present data, it should be possible to derive an approximate mass function (MF) and an estimate for the total mass of Tr14, assuming a given mass-luminosity (ML) relation. Given the uncertainty in the age (and age spread) of the cluster, we have used a set of four simplistic ML relations, each assuming a fixed-age (0.5, 1, 3, and 6 Myr) cluster and assuming that all stars brighter than a given value ($K_s = 13.00$, 13.00, 13.70, and 13.95 mag for each age, respectively) are MS objects whereas all the fainter ones are PMS. The larger caveats in these assumptions are (1) that the cluster is composed of a mixed-age rather than a fixed-age population, quite probably with a significant age spread (Sect. 3.7); (2) that the science field is largely dominated by halo stars, while the present study does not cover the halo completely (Sect. 3.6); and (3) that the transition in brightness from PMS to MS is more complex than a simple brightness limit (Ascenso et al. 2007). The extent of the consequences of these assumptions is not evaluated here. The membership problem was addressed statistically via the subtraction of the mass function of the nearby control field. Again, although we believe the control

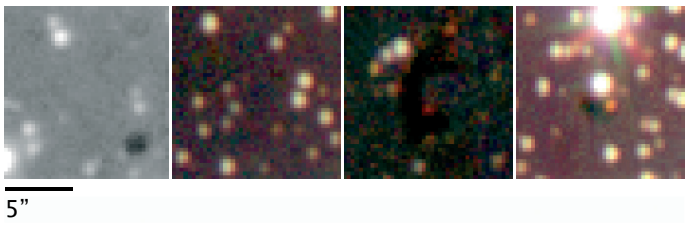

Fig. 15. Location of the proplyd candidates identified by Smith et al. (2003) in our SOFI images. From left to right, using their nomenclature: *(e)* (104339.1-593257 and 104339.8-593247), *(f)* (104402.8-593209, 104402.3-593214, and 104402.5-593218), *(g)* (104411.2-593325) and *(i)* (104359.6-593238). In the colour images blue is J, green is H, and red is K_s. The leftmost image is black and white because it is only present in our K_s-band image.

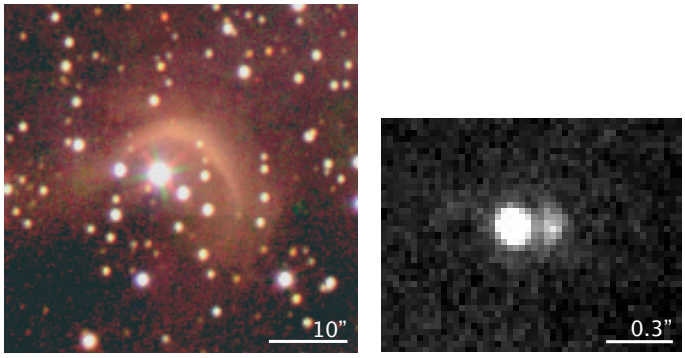

Fig. 16. *Left*: compact nebula around a B star located at $10^h44^m05\overset{s}{.}1$, $-59°33'41''$ in the surveyed field. Blue is J, green is H, and red is K_s. *Right*: extended feature ($10^h43^m57\overset{s}{.}3$, $-59°32'57\overset{''}{.}59$) detected in the L'-band. North is up and east is to the left in both images.

field to be an overestimate of the actual contamination in the science field, we have found no other reasonable method to deal with the contamination.

We applied these ML relations to our K_s-band photometry and found that the high- to intermediate-mass end of the MF flattens monotonically[10] with the assumed age from 1.97 ± 0.12 to 1.40 ± 0.12 for 0.5 and 6 Myr, respectively (a Salpeter power-law would have a slope of 1.35 in this notation). The best fits of a Kroupa (2001) IMF to the high-mass end of each derived MF yields a total mass between 8847 and 10861 $M_\odot$ for 0.5 and 6 Myr, respectively, or about 10^4 $M_\odot$ [11]. The corresponding mass of the most massive star predicted by this IMF varies between 153 and 178 $M_\odot$ for the two age limits, which compare well with the derived mass of 127 $M_\odot$ for the O2 star (Walborn et al. 2002). All these values are probably an underestimate, given 1) the relatively bright completeness limits and the over-subtraction introduced by the control field MF, and 2) the fact that we are not surveying the entire halo population (see Sect. 3.3). Regarding the slope of the MF, it is interesting to note that the value closest to Salpeter occurs for the older assumed age. Assuming, for the sake of argument, that the Salpeter MF is universal and, in particular, applicable to Tr14, this result would agree perfectly with how the science field is dominated by the halo population, which we believe could be slightly older on average than the core.

These experiments illustrate the importance of keeping the caveats in mind when deriving mass functions from photometric (NIR) data. The large uncertainties usually associated with the distance, age, age spread, membership and mass-luminosity relations in young clusters make the estimate of the mass function itself very uncertain. The comparison between different mass functions in the literature may also be somewhat affected by the assumptions made by each different author, making it difficult to assess the universality of the IMF. We hope to be able to address this matter in a future paper.

[10] The slope of the MF was determined from the bins corresponding to the MS part of the ML relation both for consistency and to avoid the errors introduced by the criteria used to distinguish between MS and PMS objects.

[11] All the masses must be corrected by a factor of $(d^2/2800^2)$, where d is the true distance to the cluster, should our adopted value be corrected in the future.

3.10. Interesting objects

3.10.1. A bright proplyd candidate?

An interesting object was revealed in the NACO thermal-IR images seen as a faint point source in H and with a faint “tail” in K_s, while it appears in the L' band and 4.05 μm NACO images as an extended object with a bright “head” and a long tail pointing directly away from the bright O2 star at the cluster’s core, HD 93129A. This object resembles the bright proplyds (photo-evaporating protoplanetary disks) found in the Orion Nebula (O’dell & Wen 1994; Bally et al. 2000; Smith et al. 2005a; Bally et al. 2005; Vicente & Alves 2005). If confirmed it would be the first proplyd-size object detected in a dense cluster harbouring high concentration of O-type stars. Perhaps revealing, is that this was also the only clear proplyd-like object found in our survey. A dedicated study of this object appears in a follow-up paper by Vicente et al. (2007).

3.10.2. Real proplyds?

Smith et al. (2003) have found numerous proplyd candidates in Hα images in the vicinities of Tr14. Some of these objects are present in the SOFI NIR images (Fig. 15), namely (e) 104339.1-593257 and 104339.8-593247 (only present in our K_s-band image), (f) 104402.8-593209, 104402.3-593214, (g) 104411.2-593325, and (i) 104359.6-593238, in Fig. 1 of SBM03 paper. The identified candidates are dark compact objects seen in silhouette against the bright nebular background. For them to be real silhouette proplyds or protoplanetary disks, they should contain an embedded star (Bally et al. 2000). At continuum NIR wavelengths, where extinction is reduced compared to optical, such a star should become obvious, even in edge-on configurations where it could be traced by scattered light. McCaughrean et al. (1998) presents optical (0.52–0.58 μm) and NIR (0.8–1.4, 1.4–1.8, and 1.9–2.1 μm) HST continuum images of the 114–426 disk, where a wavelength-dependent morphology for the polar lobes is clearly shown. As the wavelength increases, the nebulae appear to move close together, since the reduced extinction allows us to probe closer to the disk midplane, their brightness increases, and they appear to flatten from conical to slablike. Our observations are then suitable for further investigation if some of the proplyd candidates can be confirmed or rejected.

Although larger, candidates (e) (~5000 AU) and (f) resemble some of the pure silhouettes seen in Orion (Bally et al. 2000), while (i) has a “mushroom” morphology not found in Orion.

Candidate (d) has a rather irregular shape that is also not found in Orion. We do not find any evidence that these candidates are harbouring a star. Moreover, candidate (f) seems to vanish in the NIR images as if it were a piece of not very dense molecular cloud. We suggest then that the objects (e), (f), (i), and (g) are probably not proplyds but remnants of the disrupted molecular cloud similar to many others seen in the Carina Nebula.

3.10.3. A compact nebula

A relatively large compact nebula is found surrounding a late-O or early B-star (Rathborne et al. 2002; Vazquez et al. 1996) located at $10^{h}44^{m}05\overset{s}{.}1$, $-59°33'41''$ in the JHK_s SOFI images (see Fig. 16). This nebula has a width of about 2.5″ or 7000 AU and is located at about 4–11″, or 11 200–30 800 AU, from the star. It is hard not to notice that this nebula has the shape of a parabolic arc pointing in the direction of the Tr14 O2If* star, suggesting a shock front at a projected distance of 68″ or 0.9 pc, but it is hard to argue why this is the only star presenting such a shock at such a large distance. More likely is that this nebula is a compact H_{II} region associated with this young star.

3.10.4. An extended feature

A slightly extended object ($10^{h}43^{m}57\overset{s}{.}3$, $-59°32'57\overset{''}{.}59$) is detected in the NACO JHK_s images (~50 mas/pix) as a bright source elongated to the west, with size 0.″35 or 980 AU. In the L'-band (~27 mas/pix) (see Fig. 16), one starts to resolve its structure, appearing as two sources separated by 0.″16 or 450 AU. The object to the east is clearly a point source. The object to the west is fainter and elongated and it could be a younger embedded object, a photoevaporation structure, or even a relatively small shock from a jet interacting with the medium. With the present data it is not possible to say whether the two objects are even related. Multi-wavelength, high-resolution images and full 3D-spectroscopy are required to investigate the nature of these objects further.

4. Conclusions

We have presented the immediate results of a deep, NIR JHK_sL' survey of the rich cluster Tr14. Our main conclusions can be summarised as follows.

- We find that Tr14 has a well-defined core-halo structure, where less than 30% of the cluster's members reside in the core. The core seems to merge with the halo at 1.′0 (~0.8 pc at the adopted distance of 2.8 kpc) from its centre while the halo appears to have an average radius of 5′ (~4 pc at the adopted distance).
- The core has a centrally concentrated geometry that is characterised well by a King function with a core radius of 0.′17 (0.14 pc at the adopted distance) and a constant baseline of 125 pc^{-2}. Despite the unusually large number of OB stars, the surface density at zero radius (2×10^3 pc^{-2}) implies a central number density of $\sim 7.3 \times 10^3$ pc^{-3} (2.7×10^3 $M_\odot\,pc^{-3}$) that is loose in comparison with similar clusters (by factors of 40 and 100 $M_\odot\,pc^{-3}$ for NGC 3603 and Arches, respectively) and less massive clusters (e.g., by a factor of 15 for Orion).
- The fit of MS and PMS tracks to the colour–colour and colour–magnitude diagrams yields a global reddening toward the cluster of $A_v = 2.6 \pm 0.3$ mag and present no evidence for an abnormal reddening law. We find a sparse foreground population (~5 sources/arcmin^2) reddened by about $A_v = 1.4$ mag, which we suggest is not associated with Tr14 but, most likely, comprises an older population produced in the nearby young clusters of this complex.
- The colour–magnitude diagrams are compatible with ages between "zero" and ~5 Myr, although the sources from the core of the cluster appear to concentrate on the youngest isochrones, suggesting that the halo population is, on average, slightly older than the core population. The age spread inferred from our data supports a continuous star formation scenario over the last ~5 Myr.
- We constructed a background-extinction map for the cluster area derived from the colour excess of bona-fide background sources that reveals that the cluster is located in a "valley" of column density, likely carved by the O-stars in the core of the cluster. We estimate the molecular gas mass present behind the cluster to be $\sim 2.5 \times 10^3$ $M_\odot$.
- We determined a fraction of sources with excess emission in the NIR of 4% from the SOFI JHK_s data and of 35% from the NACO JHK_sL' data. We expect the latter to be a lower limit for the true NIR excess fraction in the cluster given the bright completeness limits of the L' band.
- Our data show an increasing KLF toward the faintest stars (at least) until the hydrogen burning limit, suggesting a significant low-mass population. The presence of a rich PMS population is confirmed by our colour–magnitude diagrams.
- We used a set of simplistic, fixed-age mass-luminosity relations to derive the mass-related parameters for Tr14. With these relations we find a monotonic flattening of the mass function with the assumed age that culminates in a Salpeter power-law for the high mass end and an age of 6 Myr. Despite the large caveats introduced by our somewhat strong assumptions, this result illustrates the difficulties when trying to estimate mass functions from NIR, photometric data. A fit of a scaled "normal" IMF to the cluster's mass function yields a total mass between 9000 and 11 000 $M_\odot$ for an assumed age of 0.5 and 6 Myr.
- We argue that the Smith et al. (2003) proplyd candidates that fall inside our survey (6 candidates) are not proplyds but remnants of the disrupted molecular cloud that surround the cluster.
- We find a series of interesting objects in our field that are worth future attention: a candidate photoionised proplyd best seen in the L' band, a compact nebula surrounding a B-star, and a tentative proplyd/small shock associated with a faint source.

Acknowledgements. The work of J. Ascenso has the financial support of FCT, Portugal (grant number SFRH/BD/13355/2003 and project reference POCTI/CFE-AST/55691/2004). S. Vicente acknowledges support by FCT, Portugal, through grant SFRH/BD/10285/2002, POCI 2010, and is grateful to the ESO Paranal support astronomers, Nancy Ageorges and Markus Hartung for their valuable help on the NACO data acquisition, Chris Lidman for assistance and helpful suggestions with NACO data reduction and Nuria Huélamo for every time fruitful discussions and comments.

References

Alves, J., Lada, C. J., Lada, E. A., Kenyon, S. J., & Phelps, R. 1998, ApJ, 506, 292
Ascenso, J., Alves, J., Beletsky, Y., & Lago, M. T. V. T. 2007, A&A, 466, 137
Baba, D., Nagata, T., Nagayama, T., et al. 2004, ApJ, 614, 818

Bally, J., O'Dell, C. R., & McCaughrean, M. J. 2000, AJ, 119, 2919
Bally, J., Licht, D., Smith, N., & Walawender, J. 2005, AJ, 129, 355
Bate, M. R., Bonnell, I. A., & Bromm, V. 2003, MNRAS, 339, 577
Becker, W. 1960, Z. Astrophys., 51, 49
Bessell, M. S., & Brett, J. M. 1988, PASP, 100, 1134
Binney, J., & Tremaine, S. 1987, Galactic dynamics (Princeton, NJ: Princeton University Press), 747
Brooks, K. J., Whiteoak, J. B., & Storey, J. W. V. 1998, Publ. Astron. Soc. Australia, 15, 202
Brooks, K. J., Storey, J. W. V., & Whiteoak, J. B. 2001, MNRAS, 327, 46
Brooks, K. J., Cox, P., Schneider, N., et al. 2003, A&A, 412, 751
Carpenter, J. M. 2001, AJ, 121, 2851
Carpenter, J. M., Mamajek, E. E., Hillenbrand, L. A., & Meyer, M. R. 2006, ApJ, 651, L49
Carraro, G., Romaniello, M., Ventura, P., & Patat, F. 2004, A&A, 418, 525
Cudworth, K. M., Martin, S. C., & Degioia-Eastwood, K. 1993, AJ, 105, 1822
de Graauw, T., Lidholm, S., Fitton, B., et al. 1981, A&A, 102, 257
DeGioia-Eastwood, K., Throop, H., Walker, G., & Cudworth, K. M. 2001, ApJ, 549, 578
Feinstein, A., Marraco, H. G., & Muzzio, J. C. 1973, A&AS, 12, 331
Feinstein, A., Marraco, H. G., & Forte, J. C. 1976, A&AS, 24, 389
Forte, J. C. 1978, AJ, 83, 1199
Garcia, B., Claria, J. J., & Levato, H. 1988, Ap&SS, 143, 317
Haisch, Jr., K. E., Lada, E. A., & Lada, C. J. 2001a, AJ, 121, 2065
Haisch, Jr., K. E., Lada, E. A., & Lada, C. J. 2001b, ApJ, 553, L153
Hartung, M., Lenzen, R., Hofmann, R., et al. 2003, in Instrument Design and Performance for Optical/Infrared Ground-based Telescopes, ed. M. Iye, & A. F. M. Moorwood, Proc. SPIE, 4841, 425
Herbst, W. 1976, ApJ, 208, 923
Hillenbrand, L. A., & Hartmann, L. W. 1998, ApJ, 492, 540
King, I. 1962, AJ, 67, 471
Kroupa, P. 2001, MNRAS, 322, 231
Lada, C. J., Lada, E. A., Clemens, D. P., & Bally, J. 1994, ApJ, 429, 694
Lejeune, T., & Schaerer, D. 2001, A&A, 366, 538
Lenzen, R., Hartung, M., Brandner, W., et al. 2003, in Instrument Design and Performance for Optical/Infrared Ground-based Telescopes, ed. M. Iye, & A. F. M. Moorwood, Proc. SPIE, 4841, 944
Massey, P., & Johnson, J. 1993, AJ, 105, 980
Massey, P., DeGioia-Eastwood, K., & Waterhouse, E. 2001, AJ, 121, 1050
McCaughrean, M. J., Chen, H., Bally, J., et al. 1998, ApJ, 492, L157
Megeath, S. T., Cox, P., Bronfman, L., & Roelfsema, P. R. 1996, A&A, 305, 296
Morrell, N., Garcia, B., & Levato, H. 1988, PASP, 100, 1431
O'dell, C. R., & Wen, Z. 1994, ApJ, 436, 194
Palla, F., & Stahler, S. W. 1993, ApJ, 418, 414
Penny, L. R., Gies, D. R., Hartkopf, W. I., Mason, B. D., & Turner, N. H. 1993, PASP, 105, 588
Persson, S. E., Murphy, D. C., Krzeminski, W., Roth, M., & Rieke, M. J. 1998, AJ, 116, 2475
Rathborne, J. M., Burton, M. G., Brooks, K. J., et al. 2002, MNRAS, 331, 85
Rathborne, J. M., Brooks, K. J., Burton, M. G., Cohen, M., & Bontemps, S. 2004, A&A, 418, 563
Rieke, G. H., & Lebofsky, M. J. 1985, ApJ, 288, 618
Rousset, G., Lacombe, F., Puget, P., et al. 2003, in Adaptive Optical System Technologies II, ed. P. L. Wizinowich, & D. Bonaccini, Proc. SPIE, 4839, 140
Sanchawala, K., Chen, W.-P., Lee, H.-T., et al. 2007, ApJ, 656, 462
Savage, B. D., & Mathis, J. S. 1979, ARA&A, 17, 73
Smith, N., Egan, M. P., Carey, S., et al. 2000, ApJ, 532, L145
Smith, N., Bally, J., & Morse, J. A. 2003, ApJ, 587, L105
Smith, N., Bally, J., & Brooks, K. J. 2004, AJ, 127, 2793
Smith, N., Bally, J., Licht, D., & Walawender, J. 2005a, AJ, 129, 382
Smith, N., Stassun, K. G., & Bally, J. 2005b, AJ, 129, 888
Smith, R. G. 1987, MNRAS, 227, 943
Spitzbart, B. D., & Wolk, S. J. 2004, in Optimizing Scientific Return for Astronomy through Information Technologies, ed. P. J. Quinn, & A. Bridger, Proc. SPIE, 5493, 584
Stahler, S. W., & Palla, F. 2005, The Formation of Stars ed. S. W. Stahler, & F. Palla, 865
Stolte, A., Brandner, W., Brandl, B., & Zinnecker, H. 2006, AJ, 132, 253
Sung, H., & Bessell, M. S. 2004, AJ, 127, 1014
Tapia, M., Roth, M., Marraco, H., & Ruiz, M. T. 1988, MNRAS, 232, 661
Tapia, M., Roth, M., Vázquez, R. A., & Feinstein, A. 2003, MNRAS, 339, 44
Tapia, M., Persi, P., Bohigas, J., Roth, M., & Gómez, M. 2006, MNRAS, 367, 513
Teixeira, P. S., Fernandes, S. R., Alves, J. F., et al. 2004, A&A, 413, L1
The, P. S., Bakker, R., & Antalova, A. 1980, A&AS, 41, 93
Townsley, L. K. 2006, ArXiv Astrophysics e-prints
Turner, D. G., & Moffat, A. F. J. 1980, MNRAS, 192, 283
Vazquez, R. A., Baume, G., Feinstein, A., & Prado, P. 1996, A&AS, 116, 75
Vicente, S., Alves, J., & Ascenso, J. 2007, in preparation
Vicente, S. M., & Alves, J. 2005, A&A, 441, 195
Walborn, N. R. 1973, ApJ, 179, 517
Walborn, N. R., Howarth, I. D., Lennon, D. J., et al. 2002, AJ, 123, 2754